

MODEL REDUCTION OF A PARAMETRIZED SCALAR HYPERBOLIC CONSERVATION LAW USING DISPLACEMENT INTERPOLATION

DONSUB RIM* AND KYLE T. MANDLI*

Abstract. We propose a model reduction technique for parametrized partial differential equations arising from scalar hyperbolic conservation laws. The key idea of the technique is to construct basis functions that are local in parameter and time space via displacement interpolation. The construction is motivated by the observation that the derivative of solutions to hyperbolic conservation laws satisfy a contractive property with respect to the Wasserstein metric [Bolley et al. *J. Hyperbolic Differ. Equ.* 02 (2005), pp. 91-107]. We will discuss the approximation properties of the displacement interpolation, and show that it can naturally complement linear interpolation. Numerical experiments illustrate that we can successfully achieve the model reduction of a parametrized Burgers' equation, and that the reduced order model is suitable for performing typical tasks in uncertainty quantification.

1. Introduction. Although reduced order models (ROMs) have been successfully constructed for various partial differential equations (PDEs), existing projection-based methods [5, 17, 3] are often ineffective when applied directly to problems governed by hyperbolic PDEs, and the development of ROMs for hyperbolic conservation laws still is in its early stages. The main obstacle stems from the fact that the energy of the solution is typically concentrated at different spatial locations for different time or parameter values [32, 1, 8]. Put in other terms, the Kolmogorov N -width decays slowly with respect to the dimension of the reduced basis for hyperbolic problems [16, 37]. Due to this slow decay, the construction of a global basis appears difficult.

In this paper, we build on previous works [31, 30] to propose a procedure which constructs a basis that is *local* in the parameter-time space, that neither requires additional queries to the high-fidelity model (HFM), nor utilizes adaptive procedures during the online stage of the ROM. In our approach, rather than finding a low-rank approximation for the snapshots directly, we compute the *transport maps* between the snapshots in order to find a low-dimensional structure in these transport maps. Our technique shares common features with recently proposed methods for extracting low-dimensional transport structures to be used for model reduction [25, 26, 31, 35, 36, 30].

This key idea is closely related to problems arising in optimal transport. In particular, we will make use of an interpolation procedure called *displacement interpolation* in the optimal transport literature [34, 33]. In a single spatial dimension (1D), this transport map can be computed explicitly by employing the simplest solution to the Monge-Kantorovich problem [19] called *monotone rearrangement* [2]. We will derive a variant of monotone rearrangement, guided by a crucial relation between scalar conservation laws and optimal transport observed in [6].

In justifying our construction, we find that the displacement interpolant itself has very general approximation properties. In some sense, this approximation is *dual* to linear approximation, when one views it as a linear approximation in the dependent variable in a natural coordinate transform. We make this explicit in [section 5](#) and propose a more general form for approximation, one that expands the transport map in some suitable basis [\(5.17\)](#), as opposed to the usual linear approach [\(5.16\)](#). The latter underlies many prevailing numerical methods in dimensionality reduction, e.g., singular value decomposition (SVD) [18, 14], basis pursuit [11] or generalized

*Department of Applied Physics and Applied Mathematics, Columbia University, New York, NY 10027 (dr2965@columbia.edu, kyle.mandli@columbia.edu).

polynomial chaos (gPC) [37].

This paper is organized to guide the reader through the step-by-step construction of the reduced order model. The key steps are as follows.

- Step 1. Discretization of the parameter-time space (section 3)
- Step 2. Construction of local basis using displacement interpolation (section 4)
- Step 3. Construction of the ROM via projection (section 6)
- Step 4. Dimensionality reduction using standard techniques (section 6)

In summary, we first obtain a discretization of the parameter-time space that satisfies the so-called *signature condition* (Condition 3), then we construct a basis that is local with respect to this discretization. At this stage, we may construct a ROM by projecting the PDE to this basis. Finally, we further reduce this basis using standard projection techniques such as proper orthogonal decomposition (POD).

In section 5 we will discuss the approximation properties of the displacement interpolation that will yield more insight into the local basis construction procedure. Then in section 7 we will illustrate that the ROM can then be used reliably for common tasks in uncertainty quantification (UQ) by applying Monte Carlo sampling on the constructed ROM.

2. Parametrized Burgers' equation. Throughout this paper, we will consider the example of a parametrized Burgers' equation, which was used as a benchmark problem in [9, 8, 12, 27, 28]:

$$(2.1) \quad \begin{aligned} \frac{\partial u}{\partial t} + \frac{\partial}{\partial x} \left(\frac{1}{2} u^2 \right) &= 0.02 e^{-\mu_2 x}, \quad \text{for } (x, t) \in (0, 100) \times (0, 50) \\ u(x, 0) &= 0, \\ u(0, t) &= \mu_1, \end{aligned}$$

where μ_1 is the incoming boundary condition. The values μ_1 and μ_2 are drawn from the parameter space \mathcal{M} ,

$$(2.2) \quad \boldsymbol{\mu} = (\mu_1, \mu_2) \in \mathcal{M} = [3, 9] \times [0.02, 0.075].$$

We will denote the solution to (2.1) with given parameter values $\boldsymbol{\mu}$ by

$$(2.3) \quad u(x, t; \boldsymbol{\mu}) = u(x, t; \mu_1, \mu_2).$$

The HFM will use the finite volume method (FVM) [20] to solve the equation, with the uniform finite volume cell width $\Delta x = 0.4$ amounting to $N = 250$ total number of cells, and time-step $\Delta t = 0.0125$. The finite volume cell at time t_n will be denoted by,

$$(2.4) \quad U_{i,n} := \frac{1}{\Delta x} \int_{x_{i-1/2}}^{x_{i+1/2}} u(x, t_n) dx.$$

The time-step update for the HFM is given by

$$(2.5) \quad U_{i,n+1} = U_{i,n} - \frac{\Delta t}{\Delta x} (\mathcal{F}[U_{i+1,n}] - \mathcal{F}[U_{i,n}]) + \Delta t (0.02 e^{\mu_2 x_i}),$$

where Godunov's method will be used to compute the numerical flux \mathcal{F} . Since our solution will not have positive jump discontinuities, we will not apply the entropy fix in the time-step updates, even though it would be easy to include the fix if needed.

The HFM will be run for 9 parameter values in the set \mathcal{M}_0 ,

$$(2.6) \quad (\mu_1, \mu_2) \in \mathcal{M}_0 \equiv \{3, 6, 9\} \times \{0.02, 0.05, 0.075\}.$$

A few of the computed solutions are plotted in Figure 1.

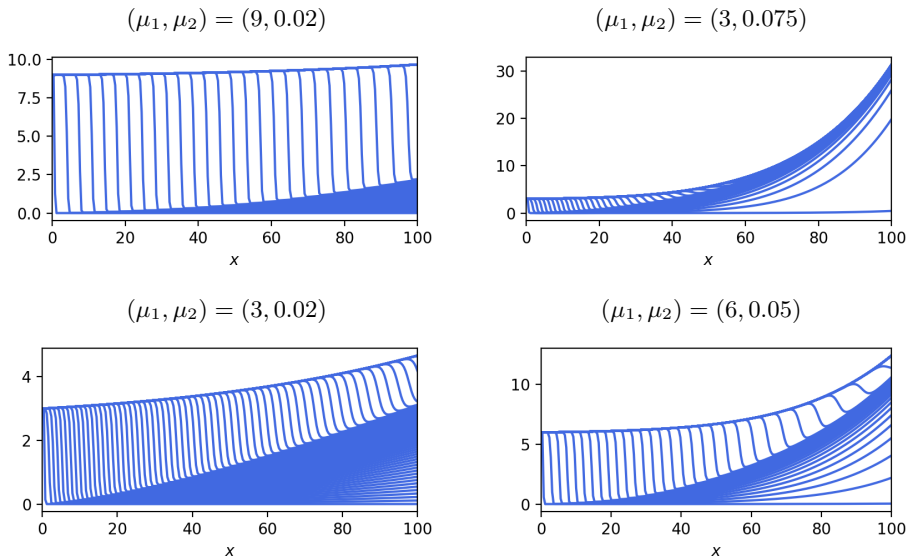


Fig. 1: HFM solutions using the finite volume method (2.5) for various parameter values, plotted every 60 time-steps.

3. Definitions and notations. In this section, we will set up definitions and notations related to the discretization of the parameter-time space, as well as those related to displacement interpolation. They will be used throughout this paper.

3.1. Parameter-time elements. Since our ROM will depend on basis functions that are local in parametric variables $\{\mu_1, \mu_2\}$ and time variable t , we will first discretize the parameter-time space. We will make use of a Delaunay triangulation for its simplicity, although this is not the only choice.

Let us first denote the entire parameter-time space by \mathcal{M}_T ,

$$(3.1) \quad \mathcal{M}_T = \{(\mu_1, \mu_2, t) : \mu_1 \in [3, 9], \mu_2 \in [0.02, 0.075], t \in [0, 50]\}.$$

We will proceed by partitioning \mathcal{M}_T as follows.

- We compute the Delaunay triangulation over the parameter space \mathcal{M} (2.2). The ℓ -th triangle in this triangulation will be denoted by \mathcal{T}^ℓ and is designated by three points $\{\boldsymbol{\mu}_{j_{\ell,1}}, \boldsymbol{\mu}_{j_{\ell,2}}, \boldsymbol{\mu}_{j_{\ell,3}}\} \subset \mathcal{M}_0$ in the parameter space. That is,

$$(3.2) \quad \mathcal{T}^\ell := (\text{convex hull of } \{\boldsymbol{\mu}_{j_{\ell,1}}, \boldsymbol{\mu}_{j_{\ell,2}}, \boldsymbol{\mu}_{j_{\ell,3}}\})$$

The triangulation we will use is plotted in Figure 2.

- We will extend the triangle \mathcal{T}^ℓ as an element over the parameter-time space by selecting a subset of the time-steps $\{t_{n_m}\} \subset \{t_n\}$

$$(3.3) \quad \mathcal{E}_m^\ell := \mathcal{T}^\ell \times [t_{n_m}, t_{n_{m+1}}].$$

A diagram of such an element is plotted in Figure 3.

- Nodes (or vertices) of \mathcal{E}_m^ℓ are the points in parameter-time space,

$$(3.4) \quad \mathcal{N}(\mathcal{E}_m^\ell) := \{\boldsymbol{\mu}_{j_{\ell,1}}, \boldsymbol{\mu}_{j_{\ell,2}}, \boldsymbol{\mu}_{j_{\ell,3}}\} \times \{t_{n_m}, t_{n_{m+1}}\}.$$

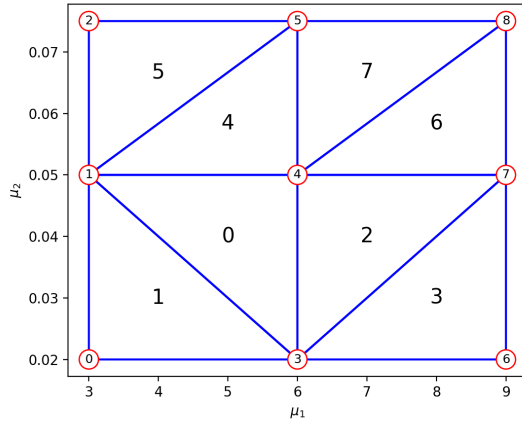


Fig. 2: Plot of the triangulation defined in (3.2) used to discretize the parameter space \mathcal{M} (2.2). The index ℓ is displayed in the interior of each \mathcal{T}^ℓ , and the index of parameter values in \mathcal{M}_0 (2.6) is displayed at the nodes of these triangles.

Note that each of these nodes can be related to the solution to (2.1). To each member of $\mathcal{N}(\mathcal{E}_m^\ell)$ there corresponds a function of the spatial variable x ,

$$(3.5) \quad u(x, t_*; \boldsymbol{\mu}_*) \quad \text{where } (\boldsymbol{\mu}_*, t_*) \in \mathcal{N}(\mathcal{E}_m^\ell).$$

Since the HFM solution will be computed for each $\boldsymbol{\mu} \in \mathcal{M}_0$ (2.6) during the offline-phase, we assume that we have an accurate approximation to the x -dependent function (3.5) via the HFM (2.5).

- The indices ℓ and m will also be used as functions,

$$(3.6) \quad \begin{cases} \ell(\boldsymbol{\mu}) = \ell(\mu_1, \mu_2) := \min\{\ell \text{ for which } \boldsymbol{\mu} \in \mathcal{T}^\ell\}, \\ m(n) := m_n := m \text{ for which } t_n \in [t_{n_m}, t_{n_{m+1}}]. \end{cases}$$

For example, given any point $(\boldsymbol{\mu}, t) \in \mathcal{M}_T$, we can compute $\ell = \ell(\boldsymbol{\mu})$ and $m = m_n$ which will allow us to find the parameter-time element the point belongs to, i.e $(\boldsymbol{\mu}, t) \in \mathcal{E}_m^\ell$.

- Time-partition $[t_{n_m}, t_{n_{m+1}}]$ for \mathcal{E}_m^ℓ will be given by the following m_n and n_m ,

$$(3.7) \quad \begin{cases} m_0 = 0, \\ m_n = 1 + \lceil \frac{n-1}{20} \rceil \text{ if } n > 0, \end{cases} \quad \begin{cases} n_0 = 0, \\ n_m = 1 + 20(m-1) \text{ if } m > 0. \end{cases}$$

Apart from the first partition $m = 0$, the time partition will contain 20 HFM time-steps.

The main motivation for this discretization is to define a basis which is to be used by the ROM locally in \mathcal{E}_m^ℓ , as we will describe in section 6.

We chose \mathcal{E}_m^ℓ to share the time-coordinates $\{t_{m_n}\}$ across all parameters $\boldsymbol{\mu} \in \mathcal{M}$ for the simplicity of exposition and implementation. But a more flexible set of elements will be better suited in practice for two important reasons: one, to satisfy

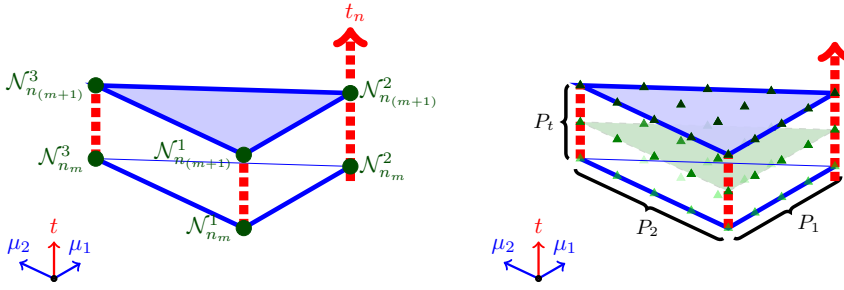


Fig. 3: A diagram of \mathcal{E}_m^ℓ (left) and the uniform interpolation points, as denoted by triangles (right). The dashed lines imply that the time-steps taken by the HFM can be finer than the height of \mathcal{E}_m^ℓ .

a stability condition (defined in subsection 4.2, Condition 3) and two, to obtain an optimal number of basis functions through dimensionality reduction. The construction of elements that satisfy the two conditions once the parameter space is discretized is straightforward: we believe the main difficulty lies in the discretization of the parameter space. Such difficulties are numerous and challenging, especially in higher dimensions, but they are not the main focus of this paper.

3.2. Displacement interpolation. The notion of *displacement interpolation* is crucial for the success of our model reduction. It originally appeared in the optimal transport literature, and is also called *McCann's interpolation* since it was devised in the study of attracting gas models in the seminal work of McCann [23]. *Monotone rearrangement* is a simple solution to the Monge-Kantorovich optimal transport problem [19] between two Borel probability distributions over \mathbb{R} . In our context, the two distributions will be taken simply as two functions in $\mathcal{C}^1(\mathbb{R})$. The solution is a transport map that deforms one function to the other, and displacement interpolation is an interpolation procedure over the transport maps, as opposed to interpolation over the functions themselves. For a more comprehensive discussion, we refer the reader to the standard references [33, 34].

Here, we will follow the definitions and notations of [30]. There, the displacement interpolation between two functions of arbitrary sign is defined as the monotone rearrangement between positive parts and negative parts of the two functions, but we will only need interpolation of two non-negative functions (equation (2.18) in [30]).

- The *displacement interpolant* between two non-negative functions u_1 and u_2 by monotone rearrangement will be denoted by,

$$(3.8) \quad \mathcal{I}(u_1, u_2; \alpha) \quad \text{for } 0 \leq \alpha \leq 1.$$

In a setting when $u_1, u_2 > 0$ are both smooth functions in $\mathcal{C}^\infty(\mathbb{R})$,

$$(3.9) \quad \mathcal{I}(u_1, u_2; \alpha) = u_2((1 - \alpha)x + \alpha M(x)) \quad \text{where } M'(x) = \frac{u_1(x)}{u_2(M(x))},$$

and the map $M(x)$ solves the Monge-Kantorovich problem:

$$(3.10) \quad \begin{aligned} \text{find } M : \mathbb{R} \rightarrow \mathbb{R} \text{ that minimizes } & \int_{\mathbb{R}} |x - M(x)| u_1(x) dx, \\ \text{subject to } & u_1(M(x)) = u_2(x). \end{aligned}$$

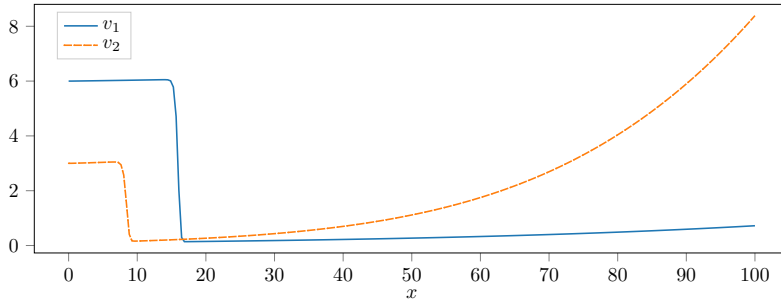


Fig. 4: Two example functions v_1 and v_2 . They are HFM solutions at parameter and time values (3.5), $(\mu_1, \mu_2, t) = (3, 0.05, 5)$ and $(\mu_1, \mu_2, t) = (6, 0.02, 5)$, respectively.

- The displacement interpolation between multiple functions is a natural extension of (3.8), and will be denoted by,

$$(3.11) \quad \mathcal{I}(u_1, u_2, u_3, u_4; \boldsymbol{\alpha}).$$

Throughout this paper the parameters $\boldsymbol{\alpha}$ will be three-dimensional,

$$(3.12) \quad \boldsymbol{\alpha} = (\mu_1, \mu_2, t),$$

and the functions $\{u_j\}$ will be the HFM approximations to (3.5).

Displacement interpolation provides a natural means of obtaining a smooth deformation between functions whose energy is concentrated in different spatial locations. When linear interpolation is applied, there is an *instant* transfer of energy across large distances, which appears unnatural for hyperbolic problems. Such behavior is automatically built into standard projection-based model reduction, as recognized early on in [32]. Coincidentally, precisely this difference in behavior led to the notion of using interpolation in the transport map rather than the function itself in optimal transport literature [23].

Perhaps an example of displacement interpolants that will be familiar to the reader will be the two-parameter family of displacement interpolants that result in the wavelet basis [13]. Taking a mother-wavelet along with its dilates and translates as the three functions and performing displacement interpolation, one obtains the wavelet basis functions up to scalar multiples.

4. Construction of local basis. As the first step in our model reduction, we generate a local basis which can represent the solution well locally in the parameter-time space. Displacement interpolation is an indispensable tool in our development, and its adaptation will be used to obtain the desired basis functions.

4.1. Displacement interpolation by pieces and signature. In this section, we define an adaptation of the usual displacement interpolation by monotone rearrangement denoted by \mathcal{I} in (3.8) and (3.11). The functions discussed in this section will belong to a function space denoted by \mathcal{U} . We will let \mathcal{U} be the space of piecewise linear functions for simplicity. Even though our solutions $(U_{i,n})$ are approximations to solutions to (2.1) that may develop jump discontinuities due to the presence of shocks, we will assume they can be well represented by piecewise linear functions with sharp gradients, at least for the purposes of displacement interpolation. The definitions here

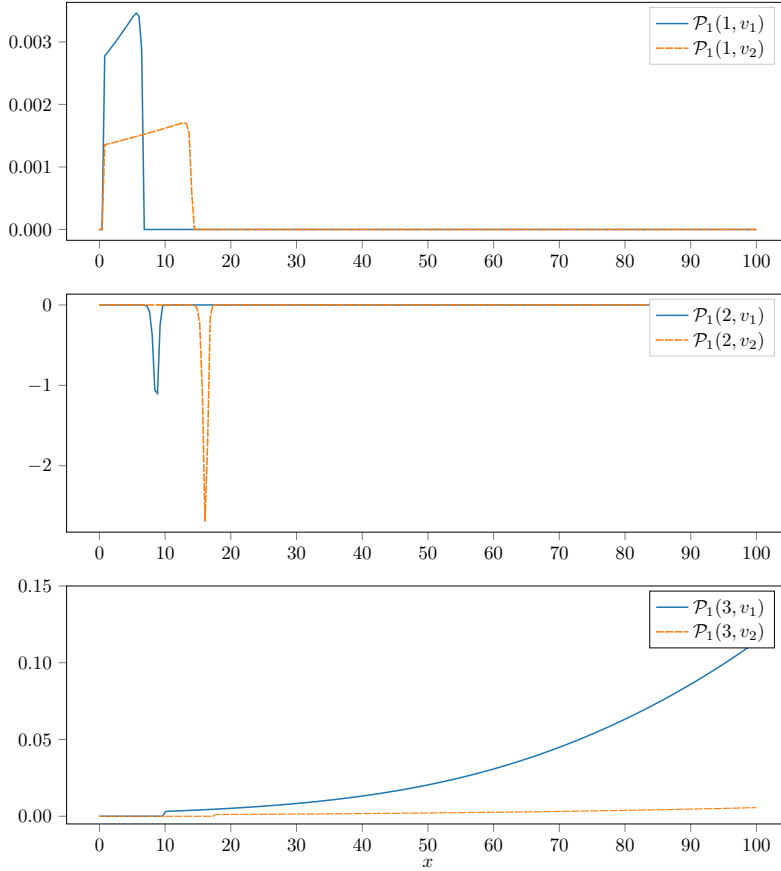


Fig. 5: The pairing of pieces $\mathcal{P}_2(v_1, v_2)$ (4.6) for the two functions v_1, v_2 in Figure 4 with same signature. Pairs $(\mathcal{P}_1(1, v_1), \mathcal{P}_1(1, v_2))$ (top), $(\mathcal{P}_1(2, v_1), \mathcal{P}_1(2, v_2))$ (middle), and $(\mathcal{P}_1(3, v_1), \mathcal{P}_1(3, v_2))$ (bottom).

extend naturally to Borel measures and distributions, but such extensions will not be discussed here.

In our adaptation, we will decompose the derivative dv/dx of a function $v \in \mathcal{U}$, into positive and negative pieces, then apply the interpolation $\mathcal{I}(\cdot)$ between corresponding pairs of pieces. For example, consider the two functions in Figure 4: the decomposition of its derivative is shown in Figure 5. The motivation for this derivation will be discussed in the following subsection 4.2.

Now we will explicitly define the procedure outlined above.

1. Define a set \mathcal{P} , which contains open subsets of the spatial domain,

$$(4.1) \quad \mathcal{S}(v) := \left\{ x : \frac{dv}{dx}(x) \neq 0 \right\}, \quad \mathcal{P}(v) := \{\text{connected components of } \mathcal{S}(v)\}.$$

Since $v \in \mathcal{C}^1(\mathbb{R})$, members of $\mathcal{S}(v)$ are open intervals in which the derivative dv/dx has the same sign.

2. Compute the spatial location of these components via the map

$$(4.2) \quad \mathbf{c}_v : \mathcal{P}(v) \rightarrow \mathbb{R} \quad \text{given by} \quad \mathbf{c}_v(P) = \frac{1}{|P|} \int_{\mathbb{R}} x \cdot \chi_P \, dx,$$

where χ_P is the characteristic function for the set P . So \mathbf{c}_v maps each open interval in $\mathcal{P}(v)$ to its centroid.

3. Denoting the natural ordering of the range(\mathbf{c}_v) by

$$(4.3) \quad \mathbf{q}_v : \mathbf{c}(\mathcal{P}(v)) \rightarrow \mathbb{N}$$

we let $\mathbf{s}_v := \mathbf{q}_v \circ \mathbf{c}_v$. Then \mathbf{s}_v maps each open interval in $\mathcal{P}(v)$ to its order of position in the domain, as counted from the left.

4. Next, we define the function which cuts off dv/dx so that it is zero outside of the designated interval in $\mathcal{P}(v)$,

$$(4.4) \quad \mathcal{P}_1(\cdot, v) : \text{range}(\mathbf{s}_v) \rightarrow \mathcal{C}(\mathbb{R}) \quad \text{given by} \quad \mathcal{P}_1(n, v) := \chi_{\mathbf{s}_v^{-1}(n)} \frac{dv}{dx}.$$

These individual functions will be called *pieces* of dv/dx .

5. Now, consider the two functions v_1 and v_2 that satisfies

$$(4.5) \quad |\text{range}(\mathbf{s}_{v_1})| = |\text{range}(\mathbf{s}_{v_2})| =: J.$$

We define a function that maps v_1 and v_2 to a set of pairs, $\mathcal{P}_2 : \mathcal{U} \times \mathcal{U} \rightarrow 2^{\mathcal{U} \times \mathcal{U}}$,

$$(4.6) \quad \mathcal{P}_2(v_1, v_2) = \bigcup_{j=1}^J \{(w_1, w_2) : w_1 = \mathcal{P}_1(j, v_1) \text{ and } w_2 = \mathcal{P}_1(j, v_2)\}.$$

For example, [Figure 5](#) shows an example of the pairs in $\mathcal{P}_2(v_1, v_2)$ for the two functions [Figure 4](#).

6. Finally, we apply the displacement interpolation \mathcal{I} to each of the pairs in $\mathcal{P}_2(v_1, v_2)$, then compute their cumulative distribution functions (CDFs).

Our strategy is to include these resulting CDFs in our local basis. The following definition summarizes the above procedure.

DEFINITION 1. Displacement interpolation by pieces for two functions $v_1, v_2 \in \mathcal{C}^1(\mathbb{R})$ is given by

$$(4.7) \quad \mathcal{I}_P(v_1, v_2; \alpha) := \bigcup_{(w_1, w_2) \in \mathcal{P}_2(v_1, v_2)} \left\{ \int_{-\infty}^x w(z) \, dz : w = \mathcal{I}(w_1, w_2; \alpha) \right\}.$$

Multi-dimensional version of \mathcal{I}_P for α follows straightforwardly from the above definition. We will always apply this interpolant on the nodes of the element \mathcal{E}_m^ℓ (3.4) so we will make use of the short-hand notation,

$$(4.8) \quad \mathcal{I}_P(\mathcal{E}_m^\ell; \alpha) := \mathcal{I}_P(u_1, u_2, u_3, u_4; \alpha), \quad \{u_j\} \subset \{u(x, t_*; \mu_*) : (\mu_*, t_*) \in \mathcal{N}(\mathcal{E}_m^\ell)\},$$

where the subset $\{u_j\}$ is chosen so that α lies in the convex hull of the corresponding nodes in $\mathcal{N}(\mathcal{E}_m^\ell)$.

The primary motivation for applying the displacement interpolation to derivatives (4.1) is due to the observation that for a class of solutions to hyperbolic conservation laws, the spatial derivative $\partial u / \partial x$ of the solution evolves along a nonlinear vector

field that coincides with that constructed by monotone rearrangement. Therefore, it appears reasonable to pursue a construction which interpolates between derivatives of the solutions. For the full proof of this, we refer the reader to [6]. Since this was proved therein only for non-increasing solutions, we will take on a slightly different viewpoint and argue below in [section 5](#) that the displacement interpolant is an approximation to an *unknown* vector field that transforms the solution across the $\{\mu_1, \mu_2, t\}$ -axis, up to first order. Since we are already able to compute the high-fidelity solution to a desired accuracy, all that we wish to accomplish is to fill in the possible states of the solution in between computed solutions using the displacement interpolant (4.7).

Another motivation for treating the pieces of the solution with positive and negative gradient separately is that for nonlinear conservation laws, the positive and negative gradients lead to very different dynamics. In the solutions to (2.1) during times $0 < t \ll 1$, the gradient of the solution du/dx have a positive piece, followed by a negative piece and a positive piece. The negative piece corresponds to a shock wave, whose propagation is governed by the Rankine-Hugoniot jump condition, where the positive pieces correspond to rarefaction waves [20]. It appears natural to approach the approximation of these behaviors separately.

The signs of each piece in (4.6) were crucial in determining the pieces in (4.1). They describe the qualitative behavior of the function and will serve a role in our stability condition to be imposed in the next subsection. We will refer to these signs through the following definition.

DEFINITION 2. We define $\mathcal{S}_1 : \mathcal{U} \rightarrow \{+1, -1\}^{|\text{range}(s_u)|}$,

$$(4.9) \quad (\mathcal{S}_1(v))_n := \text{sgn}(\mathcal{P}_1(n, v)).$$

We will call $\mathcal{S}_1(v)$ the signature of v .

For example, the signature for the two functions displayed in [Figure 4](#) are,

$$(4.10) \quad \mathcal{S}_1(v_1) = \mathcal{S}_1(v_2) = [+ , - , +].$$

4.2. Signature condition and local basis. In this section, we will construct a basis that is valid for the local element \mathcal{E}_m^ℓ using displacement interpolants (4.8). However, we must first impose some conditions on the local element \mathcal{E}_m^ℓ itself that guarantees that the construction of bases is at all possible. Consider the functions ϕ_1, ϕ_2 and ϕ_3 shown in [Figure 6](#). The three functions each have the signatures

$$(4.11) \quad \mathcal{S}_1(\phi_1) = [+ , -], \quad \mathcal{S}_1(\phi_2) = [+ , -], \quad \mathcal{S}_1(\phi_3) = [+].$$

Since ϕ_3 has a different signature, it is not an easy task to guess the location of the narrow hat function between ϕ_2 and ϕ_3 , or between ϕ_1 and ϕ_3 for that matter. One approach would be to extrapolate the hat function, but this may require significant effort to be applicable in a general setting. Instead, we will define a stability condition that prevents such difficulties. The following condition ensures that the behavior of the solution at the nodes of \mathcal{E}_m^ℓ are essentially the same.

CONDITION 3 (Signature condition). *Element \mathcal{E}_m^ℓ is said to satisfy the signature condition if each $\alpha \in \mathcal{E}_m^\ell$ lies in the convex hull of some $\mathcal{N}_0 \subset \mathcal{N}(\mathcal{E}_m^\ell)$ such that $\mathcal{S}_1(\mathcal{N}_j) = \mathcal{S}_1(\mathcal{N}_k)$ for all $\mathcal{N}_j, \mathcal{N}_k \in \mathcal{N}_0$.*

[Condition 3](#) can be also seen as a restriction on how much you can expand each element \mathcal{E}_m^ℓ without running into a significant change in the solution.

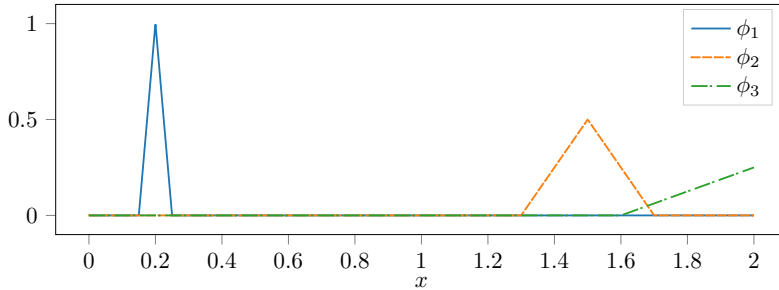


Fig. 6: Three functions ϕ_1, ϕ_2, ϕ_3 whose signature \mathcal{S}_1 is the same for the first two, but different for the last. They emulate snapshots of a hat-shaped pulse leaving the domain to the right.

Now, one natural consequence of this condition is that a more flexible form of \mathcal{E}_m^ℓ will be required to fully take advantage of the displacement interpolation. Consider the behavior of our solutions displayed in [Figure 1](#). The solution is initially $u(x, 0) = 0$ for all parameters, so the solution has null signature at $t = 0$. Then there is an immediate change of signature for the solution at positive time to $[+, -, +]$, due to the incoming boundary condition to the left and the exponential source term [\(2.1\)](#). So \mathcal{E}_0^ℓ and \mathcal{E}_1^ℓ must separate the initial condition and the first time-step. Depending on the parameter, the shock travels to the right and leaves the domain at different times depending on the parameters. Therefore to maximize the parameter-time regions covered by \mathcal{E}_m^ℓ , one must allow an unstructured discretization. This has the implication that the final time-step that could be allowed for the reduced-order model would be constrained by adhering to the uniform-in-time discretization in [\(3.3\)](#). Nonetheless, we will maintain the structured form of \mathcal{E}_m^ℓ for the simplicity of exposition and implementation.

As parameters and time are varied in the interpolation procedure \mathcal{I}_P defined above [\(4.7\)](#), the location and the sharpness of the negative gradient representing the shock are also varied smoothly. Furthermore in [\(4.7\)](#) we are constructing multiple interpolants corresponding to each pair in $\mathcal{P}_2(v_1, v_2)$ [\(4.6\)](#) separately, then including it into the set of functions on the RHS in [\(4.7\)](#). This allows more flexibility in the basis representation: for an unknown parameter value, the shock may be in a slightly different location than the computed interpolant, therefore we want to ensure that the local basis is able to represent local perturbations of the interpolant as well. This may increase the number of basis functions, but the dimensionality reduction is secondary at this stage: the goal of our basis generation is to include all basis functions that may potentially be used to represent the solution. Once we have generated such bases, we will be able to further extract a reduced basis with much smaller dimensionality (see [subsection 6.2](#) below).

Now we are ready to construct the local basis. We sample \mathcal{E}_m^ℓ uniformly at points $\{\alpha_k \in \mathcal{E}_m^\ell\}$ that are equally spaced along each $\{\mu_1, \mu_2, t\}$ -axis (i.e, a restriction of the Cartesian grid onto \mathcal{E}_m^ℓ). We will use $P_t, P_1,$ and P_2 sample points along the t -axis, μ_1 -axis and μ_2 -axis, respectively, as illustrated in [Figure 3](#). Using these sets of functions, we construct a local basis \mathcal{W}_m^ℓ corresponding to the element \mathcal{E}_m^ℓ by producing an orthonormal basis for the linear space spanned by the interpolants $\mathcal{I}(\mathcal{E}_m^\ell; \alpha_k)$ using,

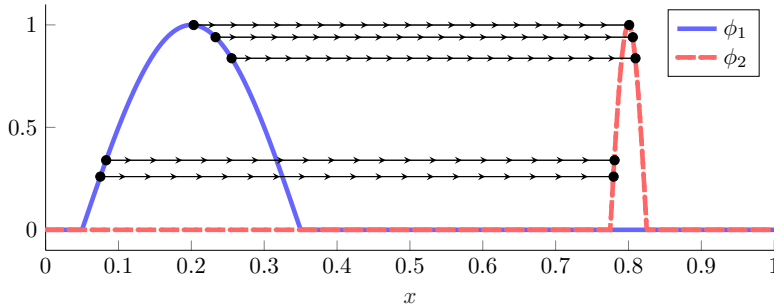


Fig. 7: Particle trajectories for the displacement interpolant (4.7).

for example, the Gram-Schmidt process,

$$(4.12) \quad \begin{cases} \text{span } \mathcal{W}_m^\ell = \text{span}\{\mathcal{I}(\mathcal{E}_m^\ell; \alpha_k)\}, \\ \langle w, w \rangle = 1, & \text{for } w \in \mathcal{W}_m^\ell, \\ \langle w_1, w_2 \rangle = 0, & \text{for } w_1, w_2 \in \mathcal{W}_m^\ell \text{ and } w_1 \neq w_2. \end{cases}$$

where $\langle \cdot, \cdot \rangle$ denotes the usual L^2 inner product. The local bases \mathcal{W}_m^ℓ will be used for Galerkin projection in section 6.

We end this section with the remark that the local basis constructions can be performed in an embarrassingly parallel manner.

5. Approximation properties of the displacement interpolant. As mentioned above, displacement interpolants are often more useful than linear interpolants for approximating wave-like phenomena. This is not so surprising upon closer inspection, as there are close relations between fluid equations such as compressible Euler’s equation and the Monge-Kantorovich problem [33]. In this section, we briefly discuss the approximation properties of the displacement interpolation \mathcal{I} (3.8) and its variant \mathcal{I}_P introduced in (4.7).

Upon discretization, \mathcal{I} can be seen as a type of a Lagrangian method such as the particle-in-cell (PIC) or large-time-step (LTS) methods. However, unlike in most applications of these methods, the velocity of the particles depend on the *dependent variable* rather than the spatial variable x : particles $x(t)$ can travel at different speeds although they are passing through the same spatial location, as evident in Figure 7. In other words, the displacement interpolant represents the dynamics of a wave profile moving through a *time-dependent* or *nonlinear* medium (5.6). In fact, we will show that the interpolant \mathcal{I} is a first-order approximation of a smooth time-dependent and possibly nonlinear velocity field in terms of the spatial variable x . On the other hand, it is also a *linear* interpolant when viewed as a function of the dependent variable (see (5.15) and (5.17) below).

To elaborate, let us write both linear interpolation and displacement interpolation \mathcal{I} as a solution to a time-dependent problem. Here time is seen merely as a parameter, and is not necessary the time variable of the underlying differential equation. Suppose that u is the solution to the problem,

$$(5.1) \quad \frac{\partial u}{\partial t} + \frac{\partial}{\partial x} (c(x, t)u) = \psi(x, t),$$

and further suppose that we know the solution u at two different times t_1 and t_2 ,

$$(5.2) \quad u(x, t_1) = u_1(x) \quad \text{and} \quad u(x, t_2) = u_2(x).$$

We will show that one obtains the linear interpolant if one assumes $c \equiv 0$, and the displacement interpolant if one assumes $\psi \equiv 0$. Throughout, we will assume that c and ψ are smooth functions of time.

5.1. Linear interpolation. Let us first assume $c \equiv 0$, then u would satisfy,

$$(5.3) \quad \frac{\partial u}{\partial t} = \psi(x, t), \quad \text{so that} \quad u(x, t) = u_1(x) + \int_{t_1}^t \psi(x, s) \, ds.$$

If $\psi(x, \cdot) \in \mathcal{C}^1([t_1, t_2])$ we can write a first order approximation of the integral above,

$$(5.4) \quad \int_{t_1}^t \psi(x, s) \, ds = \frac{u_2(x) - u_1(x)}{t_2 - t_1} (t - t_1) + \mathcal{O}(\Delta t), \quad \text{where } |t_2 - t_1| \leq \Delta t,$$

and we arrive at the linear interpolant

$$(5.5) \quad \bar{u}(x, t) = a_1(t)u_1(x) + a_2(t)u_2(x), \quad \text{where } a_1(t) = \frac{t_2 - t}{t_2 - t_1}, \quad a_2(t) = \frac{t - t_1}{t_2 - t_1}.$$

Since $|u(x, t) - \bar{u}(x, t)| \leq \mathcal{O}(\Delta t)$, \bar{u} is a first order approximation to u in t -variable.

5.2. Displacement interpolation. Let us now assume $\psi \equiv 0$, so that u solves the conservation law,

$$(5.6) \quad \frac{\partial u}{\partial t} + \frac{\partial}{\partial x} (c(x, t)u) = 0.$$

Let us assume $u > 0$, then define the CDF of $u(x, t)$,

$$U(x, t) = \int_{-\infty}^x u(z, t) \, dz \quad t_1 \leq t \leq t_2.$$

Then we can rewrite the PDE in terms via the transformation $(x, t) \leftrightarrow (y, \tau)$ where $y = U(x, t)$, $\tau = t$. Under this transformation the derivatives in (5.6) now becomes

$$(5.7) \quad \begin{aligned} \frac{\partial}{\partial x} &= \frac{\partial U}{\partial x} \frac{\partial}{\partial y} = u(x, t) \frac{\partial}{\partial y}, \\ \frac{\partial}{\partial t} &= \frac{\partial}{\partial \tau} + \frac{\partial U}{\partial t} \frac{\partial}{\partial y} = \frac{\partial}{\partial \tau} - c(x, t)u(x, t) \frac{\partial}{\partial y}, \end{aligned}$$

where the last identity comes from,

$$(5.8) \quad \frac{\partial U(x, t)}{\partial t} = \frac{\partial}{\partial t} \int_{-\infty}^x u(z, t) \, dz = \int_{-\infty}^x \frac{\partial}{\partial t} u(z, t) \, dz = -c(x, t)u(x, t).$$

Expressing the above transformation in variables y and τ ,

$$(5.9) \quad v(y, \tau) := \frac{1}{u(x(y, \tau), \tau)} \quad \text{and} \quad c(y, \tau) := c(U^{-1}(y, \tau), \tau),$$

the transformation can be summarized as,

$$(5.10) \quad \frac{\partial}{\partial x} = \frac{1}{v(y, \tau)} \frac{\partial}{\partial y}, \quad \frac{\partial}{\partial t} = \frac{\partial}{\partial \tau} - \frac{c(y, \tau)}{v(y, \tau)} \frac{\partial}{\partial y}.$$

The transformed PDE is

$$(5.11) \quad \left(\frac{\partial}{\partial \tau} - \frac{c}{v} \frac{\partial}{\partial y} \right) \left(\frac{1}{v} \right) + \frac{1}{v} \frac{\partial}{\partial y} \left(\frac{c}{v} \right) = 0.$$

Using the chain rule, and multiplying both sides by v^2 ,

$$(5.12) \quad \frac{\partial v}{\partial \tau} = \frac{\partial c(y, \tau)}{\partial y}.$$

Therefore, the evolution of $v(y, \tau)$ now solely involves the integration of $c(y, \tau)$. Integrating with respect to y and assume $c \rightarrow 0$ as $y \rightarrow 0$

$$(5.13) \quad \frac{\partial x}{\partial \tau} = c(y, \tau) \quad \text{so that} \quad x(y, \tau) = x(y, \tau_1) + \int_{\tau_1}^{\tau} c(y, s) ds.$$

where, $\tau_1 = t_1$ and $\tau_2 = t_2$. Note that this is simply a variant of (9) in [6], if we assume that $c(y, t)$ is in fact just a function of y .

This is precisely the evolution equation for the particles, whose change in speed due to the field $c(x, t)$ at x is now implicit in the moving coordinate $y = U(x, t)$. As we have observed above, displacement interpolation shifts the particles at a constant speed, and each speed is a function of y , as opposed to the original spatial variable x . Therefore, the displacement interpolant (3.8) is simply an approximation to the dynamics given by (5.13), in which the integral is approximated by a term linear in t .

Let $x_1(y) = x(y, \tau_1)$ and $x_2(y) = x(y, \tau_2)$, and if $c(y, \cdot) \in \mathcal{C}^1([\tau_1, \tau_2])$ we can write a first order approximation just as in (5.4),

$$(5.14) \quad \int_{\tau_1}^{\tau} c(y, s) ds = \frac{x_2(y) - x_1(y)}{\tau_2 - \tau_1} (\tau - \tau_1) + \mathcal{O}(\Delta\tau), \quad \text{where } |\tau_2 - \tau_1| \leq \Delta\tau,$$

The first order approximation is then simply,

$$(5.15) \quad \bar{x}(y, \tau) = a_1(\tau)x_1(y) + a_2(\tau)x_2(y), \quad \text{where } a_1(\tau) = \frac{\tau_2 - \tau}{\tau_2 - \tau_1}, a_2(\tau) = \frac{\tau - \tau_1}{\tau_2 - \tau_1}.$$

Therefore, when \mathcal{I} is applied to the snapshots from the PDE (5.6), it yields an approximation to the dynamical system (5.13), using a first order approximation to the *speed* of the evolution (5.14). This results in a particle-type method in which each particle moves at constant speed over time.

5.3. Generalized form. There is a clear analogy between (5.5) and (5.15) and the two approximations leading to a more general form. For the former, we have the usual linear approximation by separation of variables,

$$(5.16) \quad u(x, t) \approx \bar{u}(x, t) = \sum_{n=1}^{\infty} a_n(t) f_n(x),$$

for some suitable basis functions $\{f_n\}$, and for the latter, we have the approximation of the transport map that transforms some fixed function $u_0(x)$,

$$(5.17) \quad u(x, t) = u_0(x(y, t)) \quad \text{where} \quad x(y, t) \approx \bar{x}(y, t) = \sum_{n=1}^{\infty} b_n(t) g_n(y),$$

again for some basis $\{g_n\}$. For example, any linear combination of interpolation by pieces \mathcal{I}_P (4.7) could be rewritten in the form of (5.17). In effect, we have a separation of variables for the transport map. One may also view it as a series representation of the characteristics equations.

The evolution equation (5.13) is closely related to the Wasserstein metric in optimal transport [6], however the connection is no longer obvious for the more general form of the approximation above in (5.17). In other words, solution to the Monge-Kantorovich problem appears naturally as the first order approximation for the equation (5.6), but the higher order approximations are no longer solutions to this problem, as they do not move each unit of mass with constant speed, nor is it transport along multiple rays [7].

This viewpoint is already visible in the previous perspectives presented in [36, 35, 31, 26]. A common thread among them is that they naturally lead to an optimization problem. The general form here seems to offer a more constructive insight, and relates the resulting interpolation to classical approximation theory, simply by posing the problem as an approximation problem in the y -variable. This general form also can be extended to multi-dimensional settings where $x \in \mathbb{R}^n$ via the Radon transform [29, 15], since the approximation above can be applied to each direction $\omega \in S^{n-1}$ as discussed in [30]. In any case, the formulation (5.17) perhaps will serve to complement standard tools in linear approximation, such as the SVD.

6. Galerkin projection. Once the local basis has been constructed as described in section 4, we are ready to set up the Galerkin projection. The projection itself does not require special treatment, other than the fact that the basis functions will change locally with respect to parameters (μ_1, μ_2) and time t . Throughout this section, we will make use of Einstein's summation notation, in which repeated indices are summed over.

A given pair of parameter values (μ_1, μ_2) will belong to an element \mathcal{T}^ℓ (3.2) and the n -th time step t_n to an interval $[t_{m_n}, t_{m_{n+1}})$, so we will employ the notations (3.6), $\ell = \ell(\mu_1, \mu_2)$ and $m = m_n$. The local basis will be denoted by \mathcal{W}_m^ℓ (4.12), and will be valid locally in the parameter-and-time element \mathcal{E}_m^ℓ (3.3). In our numerical discretization, the basis will be represented by a matrix \mathbf{W}_m^ℓ of size $\mathbb{R}^{N \times M_m^\ell}$

$$(6.1) \quad (\mathbf{W}_m^\ell)_{ij} = W_{ij,m}^\ell \quad \text{where} \quad 1 \leq i \leq N, \quad 1 \leq j \leq M_m^\ell.$$

The matrix will be orthogonal, that is, $W_{ij,m}^\ell W_{jk,m}^\ell = \delta_{ik}$. We will be representing the finite volume solution $U_{i,n}^\ell$ (2.4) in this local basis by $r_{j,n}^\ell$,

$$(6.2) \quad r_{j,n}^\ell = W_{ij,m_n}^\ell U_{i,n}^\ell, \quad \text{and} \quad U_{i,n}^\ell = W_{ij,m_n}^\ell r_{j,n}^\ell.$$

One must also compute the *transition matrix* whenever time-stepping between \mathcal{E}_m^ℓ and \mathcal{E}_{m+1}^ℓ . That is, when $m_{n+1} \neq m_n$,

$$(6.3) \quad T_{ij,m_{n+1}} = W_{ik,m_{n+1}}^\ell W_{kj,m_n}^\ell, \quad \text{and} \quad \tilde{r}_{i,n}^\ell = T_{ij,m_{n+1}}^\ell r_{j,n}^\ell$$

which should then be used for the initial calculations in \mathcal{E}_{m+1}^ℓ , but the details are straightforward and we will omit the specifics here.

6.1. Reduced order model. In this subsection, we will restrict our attention to a fixed parameter-time element \mathcal{E}_m^ℓ and suppress the indices $\ell = \ell(\mu_1, \mu_2)$ and $m = m_n$ for the ease of notation by letting

$$(6.4) \quad W_{ij} = W_{ij,m_n}^\ell, \quad U_{i,n} = U_{i,n}^\ell \quad \text{and} \quad r_{j,n} = r_{j,n}^\ell.$$

We project the finite volume update (2.5) to the local basis $(\mathbf{W})_{ij} = W_{ij}$ of the size $\mathbf{W} \in \mathbb{R}^{N \times M}$. This yields the time-update in the new basis,

$$(6.5) \quad \begin{aligned} W_{ij}U_{i,n+1} &= W_{ij}U_{i,n} \\ &\quad - \frac{\Delta t}{\Delta x} (W_{ij}[U_{i+1,n}]^2 - W_{ij}[U_{i,n}]^2) + k W_{ij} (0.02e^{\mu_2 x_i}). \end{aligned}$$

The last two terms on the right still require computations that depend on the degree of freedom of the HFM, so we must treat them separately for performance.

- To compute the projection of the flux on to the new basis, we simply need

$$(6.6) \quad \begin{aligned} W_{ij}[U_{i,n}]^2 &= W_{ij}(W_{ki}r_{k,n})(W_{pi}r_{p,n}) \\ &= \underbrace{(W_{ij}W_{ki}W_{pi})}_{M \times M \times M} r_{k,n}r_{p,n} =: F_{jkp}r_{k,n}r_{p,n}. \end{aligned}$$

So the tensor F_{jkp} can be computed during the offline stage. This is due to the fact that the flux function $f(u) = u^2/2$ is a low-order polynomial. Fortunately, many common nonlinear hyperbolic problems have flux functions that are low-order polynomials, allowing us to employ this simple and exact reduced-basis representations of the nonlinear terms.

- To compute the projection of the source term onto these basis functions, we make use of a truncated Taylor series expansion of the exponential function up to Q -th term. Then we arrive at the approximation,

$$(6.7) \quad W_{ij} (0.02e^{\mu_2 x_i}) \approx 0.02 \underbrace{W_{ij} \frac{1}{q!} (x_i)^q (\mu_2)^q}_{M \times Q} =: S_{jq}(\mu_2)^q.$$

The S_{jq} in the RHS can be precomputed offline, and updated whenever μ_2 is determined. During the online-stage one can compute

$$(6.8) \quad (1, \mu_2, \mu_2^2, \dots, \mu_2^q, \dots, \mu_2^Q),$$

then the dot product in (6.7) can be computed with small cost.

In the case the flux terms or source terms are not in polynomial form (6.6) or are not easy to approximate as functions of the parameters (6.7), one must make use of more advanced numerical techniques, such as the discrete empirical interpolation method (DEIM) [10], Gauss-Newton with approximated tensors (GNAT) [9], or local DEIM [24], for example.

Finally, we obtain the time-update in the local basis,

$$(6.9) \quad r_{j,n+1} = r_{j,n} - \frac{\Delta t}{\Delta x} F_{jkp}r_{k,n}r_{p,n} + \Delta t S_{jq}(\mu_2)^q.$$

The system dimension for each update depends only on $M, Q \ll N$.

The computational cost for the time-stepping in the new basis now scales linearly, requiring $\mathcal{O}(N)$ floating-operations per one solve. In higher spatial dimensions the performance gain is expected to be more substantial. Nonetheless, the number of time-steps taken still depends on the dimension of the HFM and this burden is now the bottleneck of the ROM, although there may well be further model reduction possible for the time variable: this will be a topic of future investigation.

In this paper, we will compute the ROM solution (6.9) up to time $t = 12$ for ease of implementation in order to satisfy [Condition 3](#) with our structured discretization

of the parameter-time space (3.3), but this is not a restriction on the method itself, and can be lifted through an unstructured discretization of \mathcal{E}_m^ℓ as discussed above in subsection 4.2.

6.2. POD projection. It is possible to reduce dimensionality of the system (6.9) significantly further. Note that we have not so far made use of standard dimensionality reduction techniques such as the proper orthogonal decomposition (POD). We do so here by running the ROM (6.9) over many parameter values in \mathcal{M} . Then one can collect snapshots of the solution in the basis \mathcal{W}_m^ℓ , and apply the standard dimensionality reduction tools to obtain a reduced basis. This reduction does not require additional computations from the HFM, and can be done completely offline. Moreover, the elements \mathcal{E}_m^ℓ can be refined further during the computations to optimize the number of bases per time-step. The rule of thumb is that for hyperbolic problems, the number of basis required for accuracy increases linearly with the Euclidean distance in the parameter-time space, therefore more refinements will lead to a further reduction in the number of basis functions required per time-step in (6.9).

The number of bases we have obtained with unrefined-and-structured elements \mathcal{E}_m^ℓ (3.3) with the standard POD using the truncation threshold for the ratio of singular values σ_n/σ_1 set to $1\text{e-}8$, are plotted in Figure 8. We also remark that the number of bases for each element \mathcal{E}_m^ℓ appears to be independent of the size of the HFM, as long as the number of HFM time-steps included in each \mathcal{E}_m^ℓ (3.3) remains constant. More elements will be required to reach the final time, but the number of local bases functions needed at each time-step remains small, maintaining the linear scaling $\mathcal{O}(N)$.

The linear growth of number of bases observed in the number of basis for \mathcal{E}_m^ℓ in Figure 8 agrees with the rule of thumb, and can be controlled at will by the refinement of \mathcal{E}_m^ℓ . For example, if we restrict our attention to a sub-region of the parameter-time space, given by

$$(6.10) \quad \tilde{\mathcal{E}}_m := \{(\mu_1, \mu_2, t) : \mu_1 \in [6, 7], \mu_2 \in [0.06, 0.075], t \in [t_{n_m}, t_{n_{m+1}}]\} \subset \mathcal{E}_m^7,$$

the number of reduced bases required to maintain the same of level of accuracy is dramatically reduced to less than 13, as plotted in Figure 8. We will continue to employ the originally defined elements \mathcal{E}_m^ℓ here, solely for ease of illustration.

6.3. Error. A comparison of a ROM solution for a randomly chosen parameter value with its corresponding HFM solution is shown in Figure 9 up to final time $t = 12$. The HFM differs from the ROM with maximum pointwise relative error of roughly $1\text{e-}3$. The error is localized near the shock, which is to be expected.

To estimate the global error, we define the maximum point-wise relative error as,

$$(6.11) \quad E_{\text{Rel}}(\boldsymbol{\mu}) = \max_{t \in (0, 12]} \max_{x \in [0, 100]} \frac{|u_{\text{HFM}}(x, t; \mu_1, \mu_2) - u_{\text{ROM}}(x, t; \mu_1, \mu_2)|}{|u_{\text{HFM}}(x, t; \mu_1, \mu_2)|}.$$

Assuming a uniform distribution over the parameter space \mathcal{M} , we estimate the mean and the variance of the random variable $E_{\text{Rel}}(\boldsymbol{\mu})$. We use Monte Carlo sampling to obtain 10,000 samples in \mathcal{M} and compute solutions from both the ROM and the HFM, then use them to obtain the relative error (6.11). The mean and the variance are estimated as follows, indicating good accuracy:

$$\mathbb{E}[E_{\text{Rel}}(\boldsymbol{\mu})] = 3.1402\text{e-}03, \quad \text{and} \quad \text{Var}[E_{\text{Rel}}(\boldsymbol{\mu})] = 1.7852\text{e-}06.$$

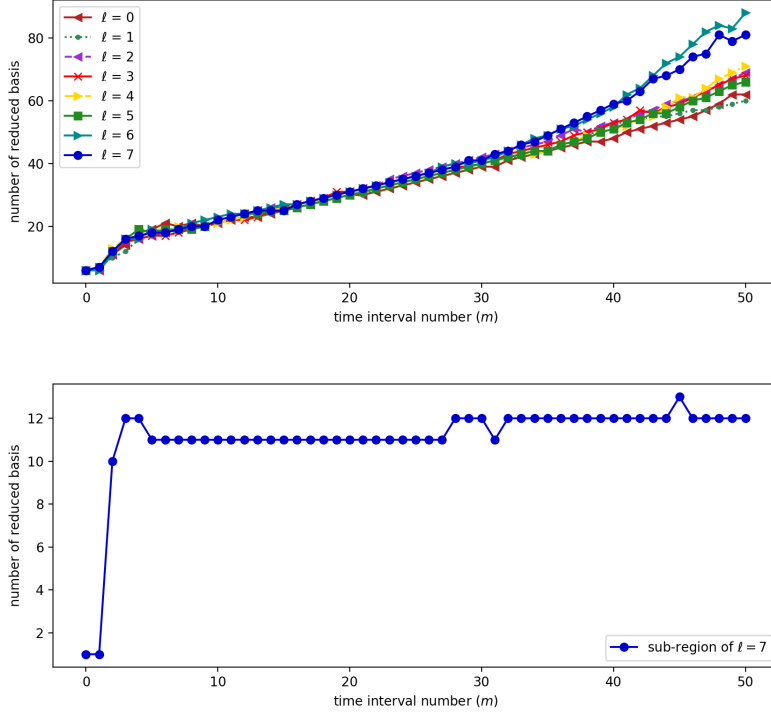


Fig. 8: Number of reduced basis for each element \mathcal{E}_m^ℓ (top) and number of further reduced basis for in the refined sub-region $\tilde{\mathcal{E}}_m$ lying in the element \mathcal{E}_m^7 (bottom).

7. Uncertainty quantification. Using the ROM developed in the previous sections, we perform a few UQ tasks in this section. We sample the parameter space uniformly, by drawing samples from

$$(7.1) \quad \boldsymbol{\mu} \sim \mathcal{U}(\mathcal{M}).$$

Using standard Monte-Carlo samples, we can easily run the ROM and extract the quantity of interest (QoI). We sampled 10,000 values of $\boldsymbol{\mu}$, then ran the ROM for each value.

- We compute the average solution and its variance, for each triangle \mathcal{T}^ℓ in the parameter space. That is, we estimate

$$(7.2) \quad \mathbb{E}_{\boldsymbol{\mu}}[u(x, t; \boldsymbol{\mu})] \quad \text{and} \quad \text{Var}_{\boldsymbol{\mu}}[u(x, t; \boldsymbol{\mu})].$$

These are plotted in [Figures 10 and 11](#). The large variance is near the shock since the shock location itself is sensitive to the change in parameter, and the large gradient near the shock incurs large variance even when the shock location varies subtly.

- We compute the two QoIs, shock location and the shock height at time $t = 12$, using the formulas for the centroid location of the n -th piece $\mathbf{q}_u^{-1} : \mathbb{N} \rightarrow$

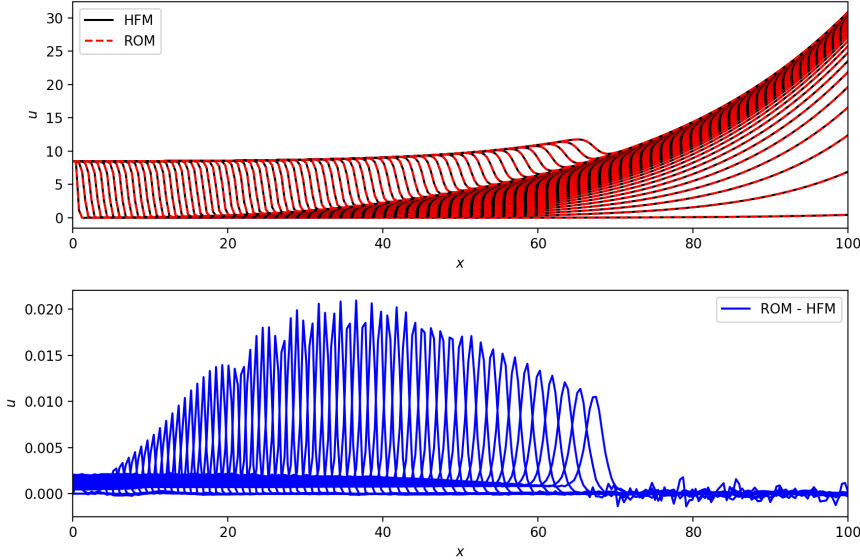


Fig. 9: Comparison between ROM and HFM (top) and the difference between the two (bottom) for parameter values $(\mu_1, \mu_2) = (8.4601, 0.0750)$. Both are plotted between every 15 time-steps.

$\mathfrak{c}(\mathcal{P}(v))$ (4.3) and the integral of the n -th piece of u , $\mathcal{P}_2(n, u)$ (4.6),

$$(7.3) \quad \begin{aligned} (\text{shock location})(t) &= \mathfrak{q}_u^{-1}(2), \\ (\text{shock height})(t) &= \int_0^{100} \mathcal{P}_2(2, u) \, dx. \end{aligned}$$

A scatter plot for the two quantities, as functions of the parameters μ_1 and μ_2 individually, are shown in Figure 12.

- The samples for the shock location and shock height can be used to compute the kernel density estimate (KDE) between the two quantities, as shown in Figure 13. It is easy to see that while the correlation between the two quantities are strong when both are small (smaller, slower shocks) the correlation weakens considerably when both are large (large, faster shocks).
- Using linear regression, we can construct a surrogate surface for the shock height and shock location as functions of $\boldsymbol{\mu}$. Using 5-th order polynomials, we can approximate the samples extremely well. This shows empirically that although the solutions develop shocks and can be discontinuous, shock location can be a smooth function of the parameters. This observation is intimately related to the approximation properties we have discussed in section 5, and has also been observed in [22].

8. Conclusion and future work. We have proposed a technique for performing a model order reduction of a scalar hyperbolic conservation law (sections 3, 4 and 6), successfully applied the technique to a parametrized Burgers' equation (2.1) and performed UQ tasks with the resulting ROM (section 7). We have also discussed

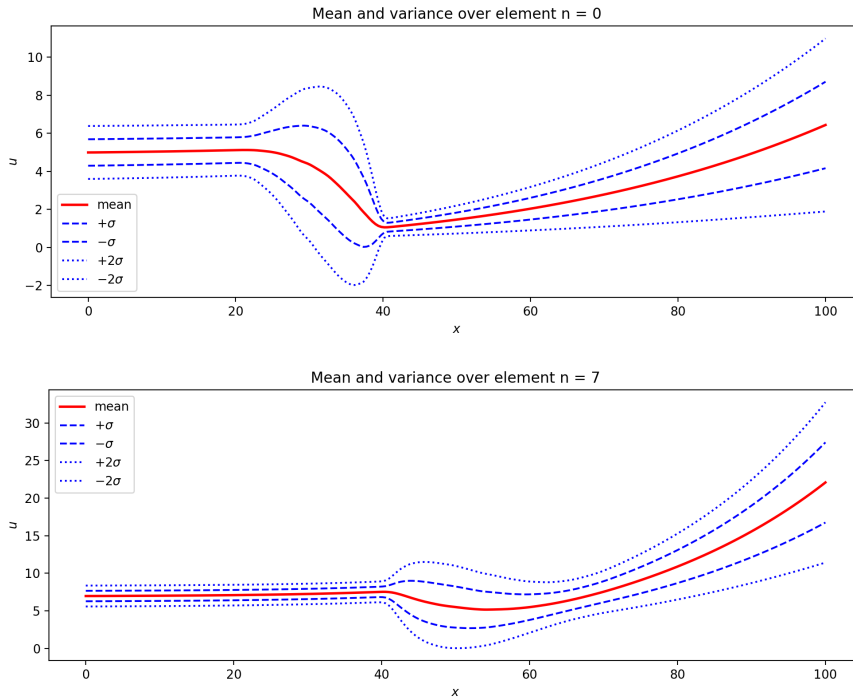


Fig. 10: Mean and variance of the ROM solution at time $t = 12$ for \mathcal{T}^0 (top) and \mathcal{T}^7 (bottom). The dashed and dotted lines indicate one and two standard deviations from the mean, respectively.

the approximation properties of the displacement interpolation (section 5) and proposed a more general form for approximation (5.17).

We believe the themes that appear in this paper naturally leads to various topics for future investigation. The dynamics in terms of the solution-dependent variable in (5.13) may be of use directly, lifting much of the burden in using the local basis for the Galerkin update (6.9). The use of the triangulations (3.2) to discretize the parameter space is also not the sole option, and other approaches would be preferable if the dimension of the parameter space is large. This would require suitably adapting the displacement interpolation (4.7).

Application to examples that require entropy fixes, and application to systems of conservation laws, dealing with more difficult source terms which appear for many applications for the shallow water equations [4, 21], generalization to multiple spatial dimensions, perhaps using the dimensional splitting approach using Radon transforms [29] are topics that are directly related to this technique. The implications of the signature condition Condition 3 can be studied further, especially for multiple dimensions. Further reduction for the time-stepping (6.9) could be explored. Finally, development and analysis of approximations of the type (5.17) and derivation of a more general approximation methods that can overcome the limitations of existing methods will also be pursued.

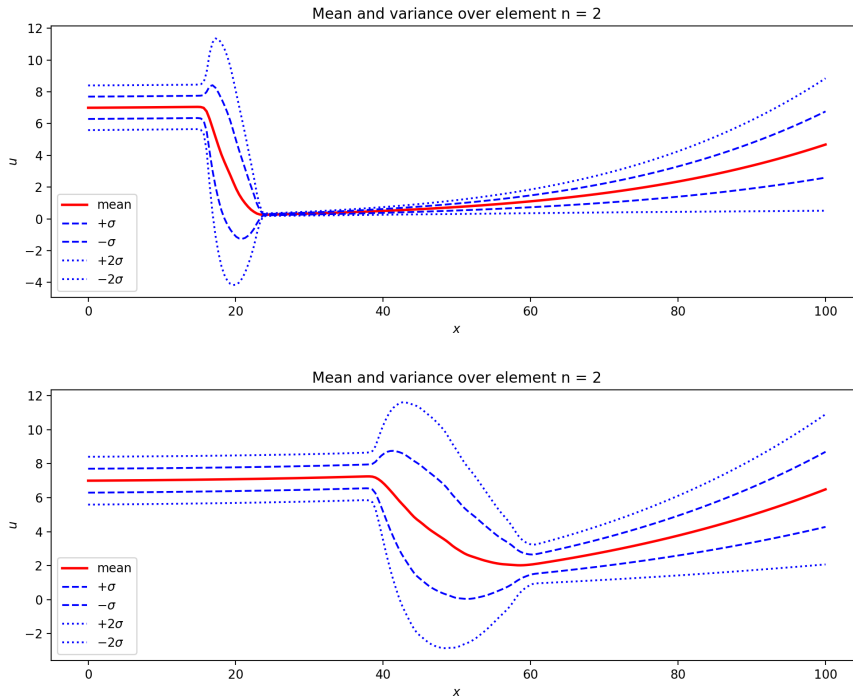


Fig. 11: Mean and variance of the ROM solution at times $t = 5$ (top) and $t = 12$ (bottom) for \mathcal{T}_2 . The dashed and dotted lines indicate one and two standard deviations from the mean, respectively.

REFERENCES

- [1] R. ABGRALL AND D. AMSALLEM, *Robust model reduction by L^1 -norm minimization and approximation via dictionaries: Application to linear and nonlinear hyperbolic problems*, *Advanced Modeling and Simulation in Engineering Sciences*, 3 (2016), p. 1.
- [2] J.-D. BENAMOU AND Y. BRENIER, *A computational fluid mechanics solution to the monge-kantorovich mass transfer problem*, *Numerische Mathematik*, 84 (2000), pp. 375–393.
- [3] P. BENNER, S. GUGERCIN, AND K. WILLCOX, *A survey of projection-based model reduction methods for parametric dynamical systems*, *SIAM Review*, 57 (2015), pp. 483–531.
- [4] M. J. BERGER, D. L. GEORGE, R. J. LEVEQUE, AND K. T. MANDLI, *The geoclaw software for depth-averaged flows with adaptive refinement*, *Advances in Water Resources*, 34 (2011), pp. 1195 – 1206. *New Computational Methods and Software Tools*.
- [5] G. BERKOOZ, P. HOLMES, AND J. LUMLEY, *The proper orthogonal decomposition in the analysis of turbulent flows*, *Ann. Rev. Fluid. Mech.*, 25 (1993), pp. 539–575.
- [6] F. BOLLEY, Y. BRENIER, AND G. LOEPER, *Contractive metrics for scalar conservation laws*, *Journal of Hyperbolic Differential Equations*, 02 (2005), pp. 91–107.
- [7] L. A. CAFFARELLI, M. FELDMAN, AND R. J. MCCANN, *Constructing optimal maps for Monge’s transport problem as a limit of strictly convex costs*, *J. Amer. Math. Soc.*, 15 (2002), pp. 1–26.
- [8] K. CARLBERG, *Adaptive h-refinement for reduced-order models*, *International Journal for Numerical Methods in Engineering*, 102 (2015), pp. 1192–1210.
- [9] K. CARLBERG, C. FARHAT, J. CORTIAL, AND D. AMSALLEM, *The gnat method for nonlinear model reduction: Effective implementation and application to computational fluid dynamics and turbulent flows*, *Journal of Computational Physics*, 242 (2013), pp. 623 – 647.
- [10] S. CHATURANTABUT AND D. C. SORENSSEN, *Nonlinear model reduction via discrete empirical*

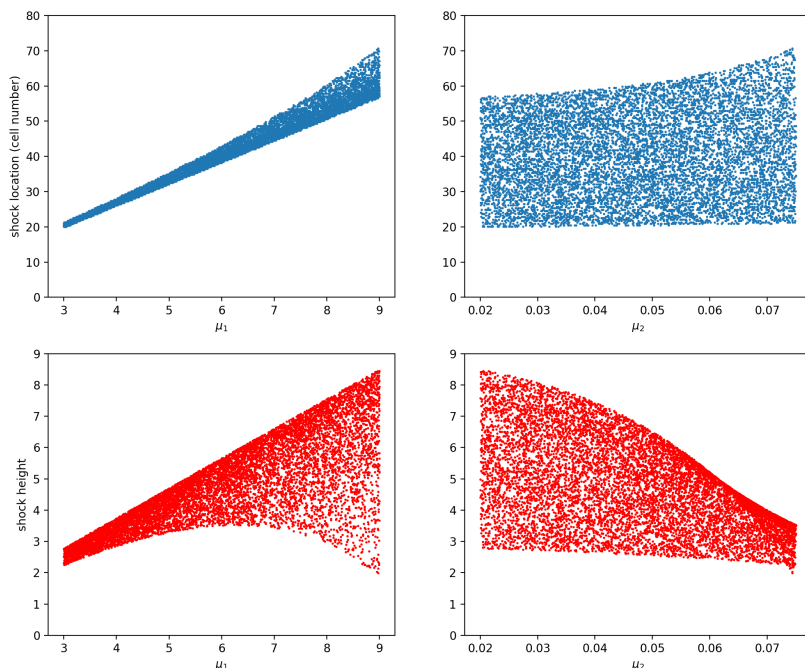


Fig. 12: Scatter plot of the shock height and shock location with respect to the parameters μ_1 and μ_2 .

- interpolation*, SIAM Journal on Scientific Computing, 32 (2010), pp. 2737–2764.
- [11] S. S. CHEN, D. L. DONOHO, AND M. A. SAUNDERS, *Atomic decomposition by basis pursuit*, SIAM Review, 43 (2001), pp. 129–159.
- [12] Y. CHOI AND K. CARLBERG, *Space-time least-squares petrov-galerkin projection for nonlinear model reduction*, Preprint, (2017), [arXiv:1703.04560](https://arxiv.org/abs/1703.04560).
- [13] I. DAUBECHIES, *Ten Lectures on Wavelets*, Society for Industrial and Applied Mathematics, 1992.
- [14] G. H. GOLUB AND C. F. VAN LOAN, *Matrix Computations (3rd Ed.)*, Johns Hopkins University Press, Baltimore, MD, USA, 1996.
- [15] S. HELGASON, *Integral Geometry and Radon Transforms*, Springer New York, New York, NY, 2011.
- [16] J. S. HESTHAVEN, G. ROZZA, AND B. STAMM, Springer Cham, Cham, Switzerland, 2016.
- [17] P. HOLMES, J. LUMLEY, AND G. BERKOOZ, *Turbulence, Coherent Structures, Dynamical Systems and Symmetry*, Cambridge University Press, 1996.
- [18] R. HORN AND C. JOHNSON, *Matrix Analysis*, Cambridge University Press, 2nd ed., 2012.
- [19] L. V. KANTOROVICH, *On a problem of Monge*, Uspekhi Mat. Nauk, 3 (1948), pp. 225–226.
- [20] R. J. LEVEQUE, *Finite Volume Methods for Hyperbolic Problems*, Cambridge University Press, Cambridge, 1st ed., 2002.
- [21] R. J. LEVEQUE, D. L. GEORGE, AND M. J. BERGER, *Tsunami modelling with adaptively refined finite volume methods*, Acta Numerica, 20 (2011), p. 211–289.
- [22] Q. LI, J.-G. LIU, AND R. SHU, *Polynomial interpolation of Burgers’ equation with randomness*, (2017), [arXiv:1708.04332](https://arxiv.org/abs/1708.04332).
- [23] R. J. MCCANN, *A convexity principle for interacting gases*, Advances in Mathematics, 128

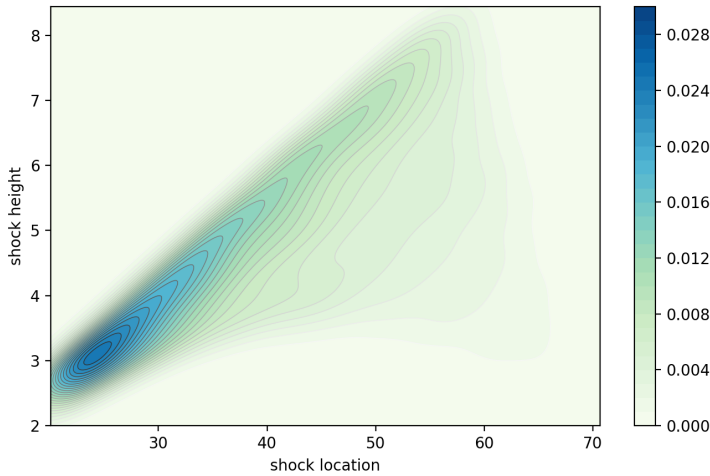


Fig. 13: Kernel density estimate (KDE) of the joint density between the shock height and shock location.

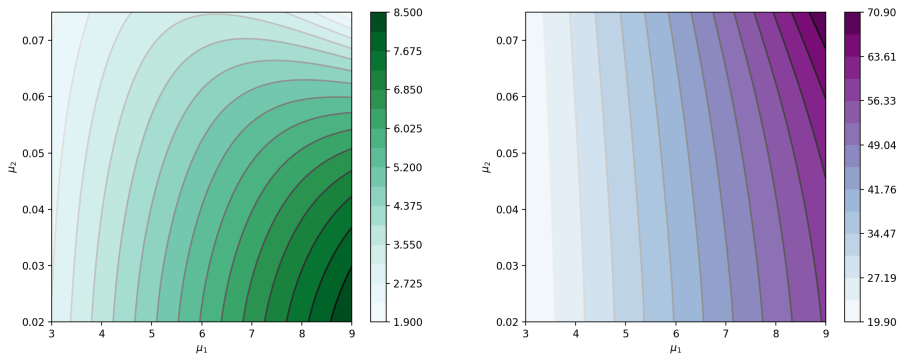


Fig. 14: Surrogate surface for the shock height (left) and shock location (right) at time $t = 12$, using polynomials of μ_1 and μ_2 orders up to 5.

- (1997), pp. 153 – 179.
- [24] B. PEHERSTORFER, D. BUTNARU, K. WILLCOX, AND H.-J. BUNGARTZ, *Localized discrete empirical interpolation method*, SIAM Journal on Scientific Computing, 36 (2014), pp. A168–A192.
- [25] J. REISS, P. SCHULZE, J. SESTERHENN, AND V. MEHRMANN, *The shifted proper orthogonal decomposition: A mode decomposition for multiple transport phenomena*, (2015), [arXiv:1512.01985](https://arxiv.org/abs/1512.01985).
- [26] J. REISS, P. SCHULZE, J. SESTERHENN, AND V. MEHRMANN, *The shifted proper orthogonal decomposition: A mode decomposition for multiple transport phenomena*, SIAM Journal on Scientific Computing, 40 (2018), pp. A1322–A1344.
- [27] M. J. REWIEŃSKI, *A trajectory piecewise-linear approach to model order reduction of nonlinear dynamical systems*, Ph.D Thesis, Massachusetts Institute of Technology, Cambridge, MA, (2003).

- [28] M. J. REWIŃSKI AND J. WHITE, *Model order reduction for nonlinear dynamical systems based on trajectory piecewise-linear approximations*, Linear Algebra and its Applications, 415 (2006), pp. 426 – 454.
- [29] D. RIM, *Dimensional splitting of hyperbolic partial differential equations using the Radon transform*, (2017), [arXiv:1705.03609](#).
- [30] D. RIM AND K. T. MANDLI, *Displacement interpolation using monotone rearrangement*, Preprint, (2017), [arXiv:1712.04028](#).
- [31] D. RIM, S. MOE, AND R. LEVEQUE, *Transport reversal for model reduction of hyperbolic partial differential equations*, SIAM/ASA Journal on Uncertainty Quantification (accepted), (2017), [arXiv:1701.07529](#).
- [32] C. W. ROWLEY AND J. E. MARSDEN, *Reconstruction equations and the Karhunen-Loève expansion for systems with symmetry*, Physica D, (2000), pp. 1–19.
- [33] C. VILLANI, *Topics in Optimal Transportation*, American Mathematical Society, Providence, RI, 2003.
- [34] C. VILLANI, *Optimal transport: old and new*, vol. 338, Springer Science & Business Media, 2008.
- [35] G. WELPER, *h and hp -adaptive Interpolation by Transformed Snapshots for Parametric and Stochastic Hyperbolic PDEs*, [arXiv:1710.11481 \[math.NA\]](#) (2017), [arXiv:1710.11481](#).
- [36] G. WELPER, *Interpolation of functions with parameter dependent jumps by transformed snapshots*, SIAM Journal on Scientific Computing, 39 (2017), pp. A1225–A1250.
- [37] D. XIU, *Numerical methods for stochastic computations : a spectral method approach*, Princeton University Press, Princeton, N.J., 2010.